Journal of Solid State Chemistry 183 (2010) 1095–1101

Contents lists available at ScienceDirect

Journal of Solid State Chemistry

journal homepage: www.elsevier.com/locate/jssc

Structural and conductivity studies of $Y_{10-x}La_xW_2O_{21}$

Anna Lashtabeg [a,*], John Bradley [b], Andrew Dicks [b], Graeme Auchterlonie [a], John Drennan [a]

[a] ARC Centre of Excellence for Functional Nanomaterials, Australian Institute for Bioengineering and Nanotechnology (AIBN), University of Queensland, St Lucia, QLD 4072, Australia
[b] CSIRO National Hydrogen Materials Alliance, CSIRO Energy Centre, 10 Murray Dwyer Circuit, Steel River Estate, Mayfield West, NSW 2304, Australia

ARTICLE INFO

Article history:
Received 12 November 2009
Received in revised form
5 March 2010
Accepted 6 March 2010
Available online 18 March 2010

Keywords:
Structural characterisation
Lanthanum tungstate
Yttria tungstate
Conductivity studies

ABSTRACT

The aim of this work was to determine structural parameters of the $Y_{10-x}La_xW_2O_{21}$ ($x=0$–10) solid solution series and investigate their electric properties. Crystallographic data shows a gradual increase in symmetry with increasing La content, as the structure evolves from orthorhombic, $Y_{10}W_2O_{21}$, towards the pseudo-cubic structure of $Y_5La_5W_2O_{21}$. The solubility limit of La_2O_3 was found to be 50% ($x=5$). Above this level two phases were observed, $La_6W_2O_{15}$ and $(La,Y)_{10+x}W_{2-x}O_{21-\delta}$. The conductivity of Y rich samples was very low, with σ of the order 2×10^{-5}–5×10^{-5} S cm^{-1} at 1000 °C, whilst ionic conductivity was observed for most La rich doped samples. The highest conductivity was observed for $La_{10}W_2O_{21}$ and its doped analogues, at 1×10^{-3}–5×10^{-3} S cm^{-1} at 1000 °C. Unit cell parameters were determined as a function of temperature from 0 to 1000°C, and thermal expansion of these materials was determined from temperature studies carried out at the Australian Synchrotron facility in Melbourne, Victoria, Australia.

1. Introduction

There has been a wealth of studies on rare earth (RE) tungsten oxides in the system RE_2O_3–WO_3 [1–3] (RE=La–Lu and Y) as a result of the wide range of applications in which these materials can be employed, such as ferroelectrics, phosphors and refractory materials. Yttria tungstates have displayed a number of interesting properties, such as fluorescence [4] and negative thermal expansion [5] while lanthanum tungstates have been intensively studied as a result of some interesting electrochemical and optical properties: $La_xWO_{3+1.5x}$, ($x\cong6$) for example is known to exhibit proton conductivity in wet hydrogen at 900 °C [6–8].

Within the composition range RE_2O_3–RE_2WO_6 where the oxygen to metal ratio, O/M, is 1.5–2, these phases are generally examples of anion deficient, fluorite-related compounds with anion deficient superstructures. The phase diagram for the La_2O_3–WO_3 system has been investigated [9] and a large number of phases have been identified, of which the 5:2 phase ($La_{10}W_2O_{21}$) is one of the phases often confused with the high temperature 3:1 phase (La_6WO_{12}), which is a stoichiometry common to most of the other RE_2O_3–WO_3 and RE_2O_3–MoO_3 systems.

Although the 5:2 phase for lanthanum tungstate is thought to have a pyrochlore-related structure [9], there is little other information on its structure and no information on its electrochemical properties in the literature, thus little is known about the structure–properties relationship in this class of materials. In contrast, the phases $Ln_{10}W_2O_{21}$ occur unambiguously over a small compositional range in the smaller lanthanides for Ln=Nd–Er, Y [10], and are known to have orthorhombic unit cells based on a distorted fluorite parent structure.

The aim of this work was to determine structural parameters of the $Y_{10-x}La_xW_2O_{21}$ ($x=0$–10) solid solution series and investigate their electric properties. Other than structural information of $Y_{10}W_2O_{21}$ [10], no other information is available on this material. The electrochemical properties of $Y_{10}W_2O_{21}$ are examined and followed by doping this material with a dissimilar sized trivalent cation onto the Y site. In this paper La was chosen, and the structural and electrochemical properties were examined as a function of dopant concentration.

2. Experimental

Fluorite-related compounds in the $Y_{10-x}La_xW_2O_{21}$ series were prepared using a standard solid state reaction of dried metal oxides, Y_2O_3, La_2O_3 and WO_3 (Sigma Aldrich), with purities $>99.95\%$. The powders were mixed by hand in an agate mortar and pestle then pressed into pellets at 1.5 tonnes/cm^2. The pellets were buried in powder inside the Pt crucible and covered with an alumina lid in order to minimise WO_3 volatisation. The samples were reacted at 1350–1600 °C for up to 72 h with intermediate regrinding and re-pelletising, with heating and cooling ramp rates of 5 °C/min. The density of most samples was very low at 50–55%. Post-reaction sintering of pellets at 1600 °C for 8 h produced densities of 55–95% of theoretical density.

* Corresponding author.
E-mail address: a.lashtabeg@uq.edu.au (A. Lashtabeg).

0022-4596/$ - see front matter © 2010 Elsevier Inc. All rights reserved.
doi:10.1016/j.jssc.2010.03.009

Initial X-ray diffraction (XRD) was performed using a Bruker D8 Advance X-ray diffractometer with Cu$K\alpha$ radiation, with 2θ scanning range 5–90° at intervals of 0.01°, and with stepping time of 6 S. Silicon obtained from Gem Dugout ($a=5.4301$ Å $\pm$ 0.0001 Å—200 mesh) was used as a standard reference material.

Synchrotron X-ray diffraction data were collected at the Australian synchrotron facilities, equipped with a Si (1 1 1) monochromator. The samples were contained in 0.5 mm quartz capillaries, and data collected at 15 keV energy and 273–1273 K temperature range. Rietveld refinement and Pawley fitting were performed using Topas Academic V4.1 refinement software. The thermal expansion data were obtained from unit cell refinement of samples to 1273 K.

Transmission electron microscopy was performed on selected specimens. Samples were prepared by dispersing powders that had been crushed under dry ethanol on to copper grids coated with holey carbon film. The instrument used was a Jeol 2100 which was operated at an accelerating voltage of 200 keV.

Two-terminal AC impedance measurements were carried out in static air with a Solarton 1260 frequency response analyser, from 1 MHz to 0.1 Hz at an oscillation amplitude of 50 mV, with ZPlot/ZView software used for data collection and data analysis. Platinum paste was painted on each pellet face, fired at 900 °C for 1 h to form electrodes, and this process repeated until the resistance across the face of the pellet was less than 0.1 Ω. The samples were allowed for 1 h equilibration time after reaching each of the 50 measured temperatures before the measurement was initiated, with half of the measurements taken at regularly spaced intervals on the $1/T$ scale on the heating part of the cycle from room temperature up to 1000 °C, and the other half at intermediate temperatures on the cooling cycle. The data were modelled using ZView software and the errors for high resistance samples was in the range 0.1–0.01% due to the simplicity of the model using only one or two RC circuits. The bulk and the grain boundary responses for these high resistance samples were not distinguishable. The samples with lower resistances and ionic components were modelled using 2–3 RC circuits in parallel with the Warburg component. The errors on the fit were in the range 1–5% with increasing complexity of the model.

Thermo-gravimetric Analysis was carried out using Mettler-Toledo TGA/DSC1 module in flowing air at 20 ml/min, with heating and cooling ramp rates of 5 °C/min and 60 min dwell time at 1000 °C. The TGA instrument was calibrated using metal standards and the equipment baseline, measured with two empty crucibles, was subtracted.

3. Results and discussion

3.1. Crystal Structure

The newly measured unit cell of $Y_{10}W_2O_{21}$ is in good agreement with Bevan et al. [10], and formed a basis for the XRD refinement of doped samples up to $x=0.25$. $Y_{10}W_2O_{21}$ itself is described as a fluorite-related superlattice of $3\times2\times2$ fluorite units with $a=15.8761$ Å, $b=10.5232$ Å and $c=10.5778$ Å, space group *Pbcn*, ICSD #35239 [10].

In the ideal fluorite structure the cations in eight-fold coordination with oxygen can be regarded as being in a chequer-board arrangement of cubes, with alternating occupied and empty polyhedra, and this arrangement of polyhedra is retained in the fluorite-related superlattice forming a three dimensional open structure (Fig. 1). In the $Y_{10}W_2O_{21}$ structure one in eight anions is absent with respect to fluorite and the cations have an average coordination number of seven, however the W cations are in sixfold coordination with O^{2-} in distorted octahedra while the Y

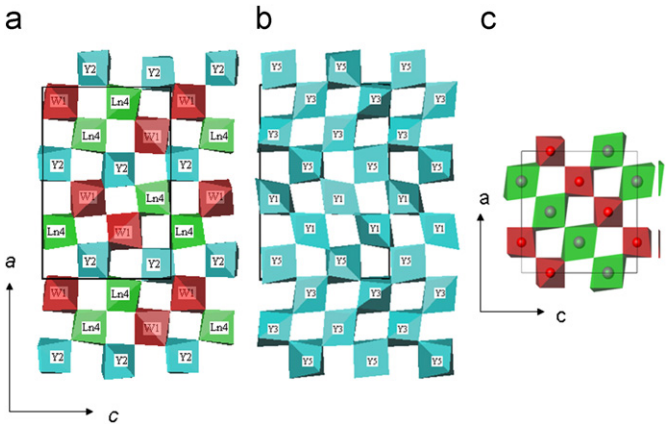

Fig. 1. (a) and (b) $Y_{10}W_2O_{21}$ viewed down the *b* axis, and showing two successive layers of cations at $y\sim0$ and $y\sim1/4$: blue 7 co-ordinate Y (Y1, Y2 and Y3), green 8 co-ordinate Y (Ln4), red 6 co-ordinate W (W1) (c) ideal cubic pyrochlore structure: red 6 co-ordinate cation, green 8 co-ordinate cation.

cations are entirely sevenfold co-ordinate in one *a*/*c* layer, and equally seven and eight-fold co-ordinate in the successive *a*/*c* layer which they share with the tungsten (Fig. 1).

Analysis of the XRD data, Fig. 3, shows that the substitution of Y^{3+} by La^{3+} forms a solid solution series, $Y_{10-x}La_xW_2O_{21}$, with no additional lines corresponding to other phases up to the lanthanum rich phase $x=7.5$, whereupon the secondary orthorhombic phase $La_6W_2O_{15}$ forms and increases in concentration with further increase in yttria substitution, indicating La solubility in the Y sublattice up until at least $x=5$, i.e. 50% substitution. The materials in the stoichiometric range of $x=0$–2.5 crystallise in the parent orthorhombic unit cell and the XRD patterns in Fig. 3 show a shift in peak position consistent with increasing unit cell size as VII co-ordinated Y^{3+} (0.96 Å) is substituted by a larger VII co-ordinated La^{3+} cation (1.10 Å) (Table 1).

The *Ln*(4) site in$Y_{10}W_2O_{21}$ is the eight co-ordinate cation site [10], however the large distances between the *Ln*4 site and O(2) and O(5) sites, suggests that sixfold-triangular-prismatic coordination can also be considered reasonable for this cation. As a result of the larger size of La^{3+} in sevenfold coordination (1.10 Å) and eight-fold coordination (1.16 Å) compared to Y^{3+} (0.96 and 1.02 Å, respectively), it is apparent that the *Ln*4 site is an ideal La acceptor and preferential eight-fold coordination of La was assumed at the outset of the Rietveld refinements.

With increasing La^{3+} content the diffraction patterns show an increase in symmetry from orthorhombic $Y_{10}W_2O_{21}$, and at $x=0.5$, $Y_5La_5W_2O_{21}$, the cell can be indexed as face centred cubic, with $a=10.873$ (1) Å, a superlattice of $2\times2\times2$ fluorite units similar to pyrochlore, $A_2B_2O_7$. Although $Y_5La_5W_2O_{21}$ may be indexed as face centred cubic from laboratory X-ray data the powder patterns show extra reflections that are systematic absences in the *Fd*-3*m* space group of pyrochlore. Synchrotron data show the asymmetry in the peak shape that is consistent with a smaller body-centred orthorhombic unit cell of $a=7.6780$ (4) Å, $b=10.8596$ (3) Å, $c=7.6767$ (3) Å, a superlattice of $\sqrt{2}\times2\times\sqrt{2}$, Fig. 2.

Indexing of the peaks for the synchrotron data strongly suggests $Y_5La_5W_2O_{21}$ belongs in the space group *Imm*2 (44), or one of the other three space groups indistinguishable by indexing in powder diffraction: *I*222 (23), $I2_12_12_1$ (24) and *Immm* (71). Initial attempts at Rietveld refinement of the synchrotron data in *Imm*2 shows that $Y_5La_5W_2O_{21}$ crystallises in a weberite type structure, A′ A″B′ B″O_7, which is very closely related to pyrochlore, however in weberite the A site cations occupy two slightly

Table 1
Unit cell of $Y_{10-x}La_xW_2O_{21}$.

x	a (Å)	b (Å)	c (Å)	V (Å^3)	Density (g/cm^3)	Density % at 1600 °C	R_{wp}	Crystal system	Space group
0	15.8777 (1)	10.5252 (1)	10.5725 (1)	1766.83(1)	5.988	57.6	5.846	Orthorhombic	*Pbcn* (60)
0.5	15.9143 (1)	10.5513 (1)	10.5914 (1)	1778.48 (2)	6.023	56.5	6.193	Orthorhombic	*Pbcn* (60)
0.75	15.9336 (1)	10.5636 (1)	10.6016 (1)	1784.42 (2)	6.040	56.7	5.905	Orthorhombic	*Pbcn* (60)
1	15.9520 (1)	10.5796 (1)	10.6123 (1)	1790.99 (1)	6.092	57.4	5.977	Orthorhombic	*Pbcn* (60)
1.5	15.9879 (1)	10.6020 (1)	10.6341 (1)	1802.53 (1)	6.145	71.0	6.190	Orthorhombic	*Pbcn* (60)
2.5	16.0725 (1)	10.6710 (1)	10.6912 (1)	1833.65 (1)	6.222	94.6	5.844	Orthorhombic	*Pbcn* (60)
5	7.6773 (2)	10.8575 (3)	7.6775 (3)	639.97 (4)	6.375	66.5	6.267	Orthorhombic	*Imma* (44)
7.5	7.7936 (1)	11.0236 (1)	7.7836 (1)	668.71 (1)	–	66.3	4.686	Orthorhombic+$La_6W_2O_{15}$	*Imma* (44)
9	7.8563 (1)	11.1068 (1)	7.8506 (1)	685.02 (1)	–	87.8	4.796	Orthorhombic+$La_6W_2O_{15}$	*Imma* (44)
10	7.8967 (1)	11.1736 (1)	7.9008 (1)	697.12 (1)	–	62.2	9.482	Orthorhombic+$La_6W_2O_{15}$	*Imma* (44)

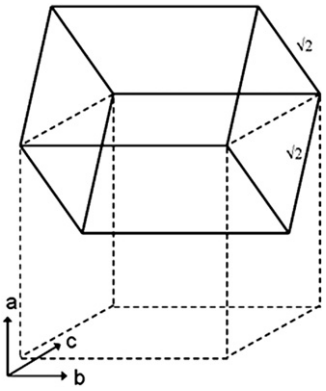

Fig. 2. Schematic of the doubled cubic, face-centred unit cell, from X-ray data (dashed lines), 2**a** 2**a** $\sqrt{2}$**a** body-centred cell from synchrotron data (solid lines).

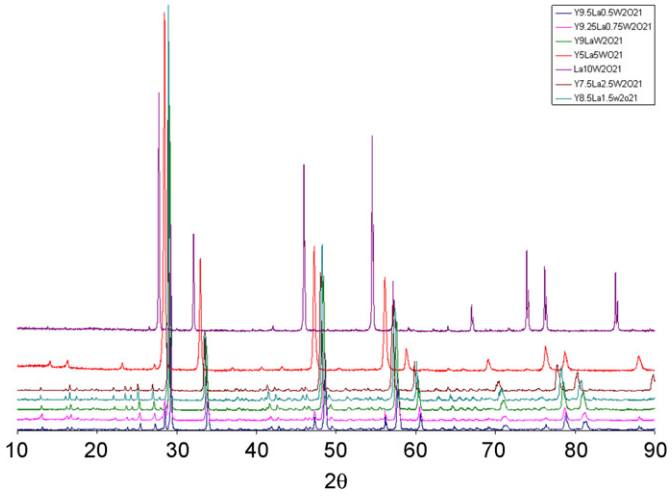

Fig. 3. X-ray diffraction plots for $Y_{10-x}La_xW_2O_{21}$, showing a related structure for all samples.

different eight-fold co-ordinate environments and the B-site cations similarly occupy two different octahedral positions (Fig. 4).

Weberite, Na_2MgAlF_7 ICSD #33507, was also initially thought to belong to space group *Imm*2 from single crystal measurements in preference to its true space group of *Imma* (74) due to extra weak *hk0* reflections in the diffractograms, but was found subsequently to belong to *Imma*, with the extra weak peaks in the diffraction pattern that suggested *Imm*2 being due to double

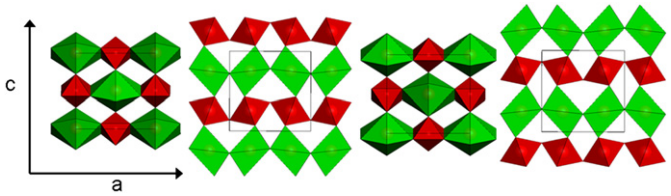

Fig. 4. Weberite structure of $Y_5La_5W_2O_{21}$.

diffraction [11], known as the Renninger effect [12]. *Imma* was thus chosen for the Reitveld analysis in this study.

Bevan et al. [10] postulated that the *Ln*(4) site, unlike other *Ln* sites, produces the same cation pattern in the structure as the W site, thus it is possible to have an exchange of cations between these two sites. With increasing La doping onto this site, the reversal of the *Ln*4 and W sites appears to occur and this may be responsible for the trend towards the pseudo-cubic, fluorite-related unit cell.

Homogeneous and random solid solutions obey Vegard's law, which states a linear dependence between composition and structural parameters [13]. Fig. 6 shows a linear relationship with composition and reduced unit cell parameters. It can be seen that with increasing La content the lattice parameters b and c progress towards the pseudo-cubic lattice seen for $Y_5La_5W_2O_{21}$. Phase density also shows a linear relationship with increasing Y^{3+} substitution by the heavier La^{3+} ion. Above $x=7.5$ a secondary phase occurs, $La_6W_2O_{15}$ also with unknown crystal structure, however, further incorporation of La into the structure is evidenced by a linear increase in the unit cell parameters.

The density of the samples, though low for Y rich samples, increases when the La content is $>10\%$ at 1600 °C. The highest measured density at 1600 °C was observed for $Y_{7.5}La_{2.5}W_2O_3$, at $\sim$95% of theoretical, a midpoint between the orthorhombic $Y_{10}W_2O_{21}$ and cubic $Y_5La_5W_2O_{21}$, indicating a possible transition point in the phase diagram for the solid solution series. Increasing the La content further produces samples with lower density.

$La_{10}W_2O_{21}$ was first identified by Yoshimura and Rouanet [9], and was thought to be a face centred cubic, pyrochlore-like structure, $La_2(La_{2/3}W_{1/3})_2O_7$. Prior to our study this compound was erroneously referred to in a number of papers as the high temperature phase La_6WO_{12} [6–8], however it has not been characterised in these papers, nor have any crystallographic patterns or data been presented. Fig. 5 shows that the composition "$La_{10}W_2O_{21}$" consists of two phases, tungsten rich $La_6W_2O_{15}$ and a weberite type phase, which is tungsten deficient compared to $Y_5La_5W_2O_{21}$. In this study this weberite phase in a fully substituted compound $x=10$ was identified to be $La_{11}W_2O_{21.5}$, La_2 $(La_{9/13}W_{4/13})_2O_{21-\delta}$. The unit cell of both compounds is very similar indicating that the La_2O_3:WO_3 ratio

of 5:2 cannot be made to be stoichiometric and the true ratio is 11:4.

Increasing the lanthanum content above 50% in $Y_{10-x}La_xW_2O_{21}$ requires La^{3+} to begin occupying the smaller sixfold co-ordinate B-sites in the Weberite structure. The La^{3+} ion in sixfold coordination has an ionic radius of 1.032 Å [14], expanding the lattice and consequently the B″ site above the tolerance factor for the smaller W^{6+} ion, ionic radius 0.60 Å VI. This expansion results in the expulsion of tungsten in the form of $La_6W_2O_{15}$ and the quantity of this impurity can be seen from the XRD data to increase with further substitution by lanthanum. The lanthanum rich phase $La_6W_2O_{15}$ was also previously reported as orthorhombic in the two La_2O_3–WO_3 phase diagram studies [9,15], with the indexed lattice parameters from [3] twice those of [15] and no space group information from either. The unit cell parameters of $La_6W_2O_{15}$ do not change across the compositional range demonstrating no yttria uptake by this phase and a very narrow solid solution range, while evidence for the continued Lanthanum uptake in the weberite structure is demonstrated by the linear increase in the unit cell parameters, Fig. 6.

3.2. Thermal Expansion

The thermal expansion coefficient (TEC) was measured in fine grades at low temperatures, 0–100 °C and in larger steps at high temperatures, 100–1000 °C. For all samples the TEC was found to be anisotropic along the *b* axis, mimicking the anisotropic unit cell expansion along the same axis. The *a* and *c* axis had a similar TEC in all samples. As is common with many materials the thermal expansion is not truly linear as a function of temperature and was seen to be lower at lower temperatures. $Y_{10}W_2O_{21}$ has a volumetric TEC of $2.75E-05\,K^{-1}$ (25–1000 °C) and $2.12E-05\,K^{-1}$ (0–100 °C). The anisotropic expansion of the *b* lattice parameter both with temperature and doping shows that it is primarily the change in this axis which progresses the structure towards tetragonal or cubic symmetry (Figs. 6 and 7).

3.3. TEM

X-ray diffraction provides us with the parent structure relationship. The cations provide most of the scattering and the strong reflections correspond to cation positions which are usually in very standard configurations. Anion positions which will determine superstructure variations do not scatter strongly and are therefore easily missed. Electron diffraction overcomes a number of these problems and can reveal the true full structure. The difficulty is however, that very small regions are examined under the beam and selectivity becomes an issue.

In Fig. 8(a) a representative electron diffraction pattern has been recorded from a sample with the nominal composition $Y_{10}W_2O_{21}$. The strong reflections that dominate the pattern can be indexed as a typical [1 1 0] zone from a face centred cubic structure. Weaker reflections between these strong 'parent structure' reflections represent a related superstructure. In this zone, three equally spaced reflections can be seen between the 000 direct beam at the centre and the 200 type reflections of the face centred cubic parent. Perpendicular to this a single reflection intersects from 000 to 220. Although it appears that there is a row of reflections in this space, these appear because the upper Laue

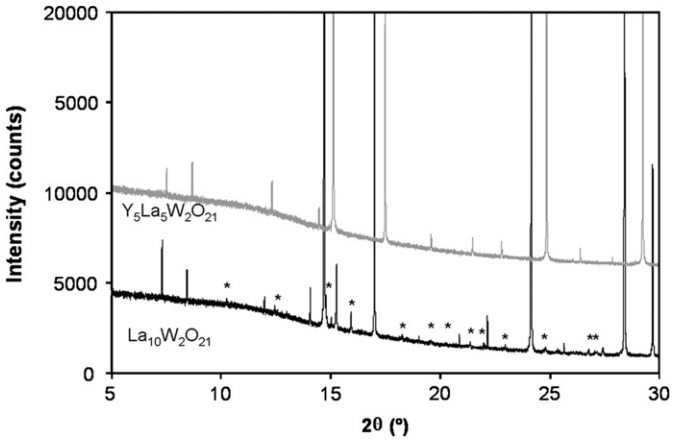

Fig. 5. Synchrotron XRD data showing $La_6W_2O_{15}$ impurity (*) in the $La_{10}W_2O_{21}$ phase, that is not seen in $Y_5La_5W_2O_{21}$.

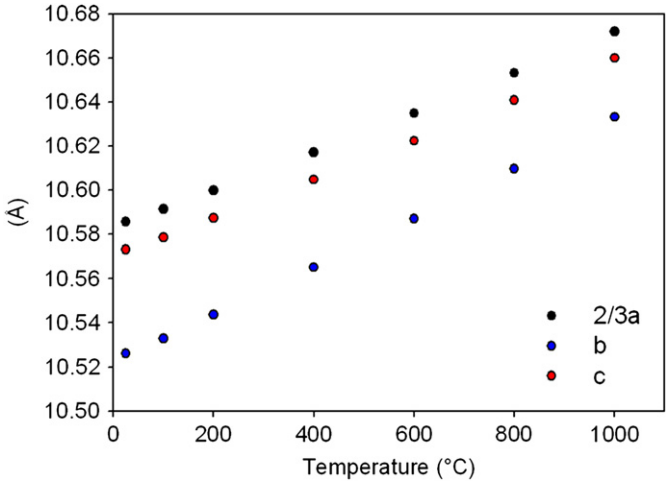

Fig. 7. Change in unit cell parameters as a function of temperature in $Y_{10}W_2O_{21}$.

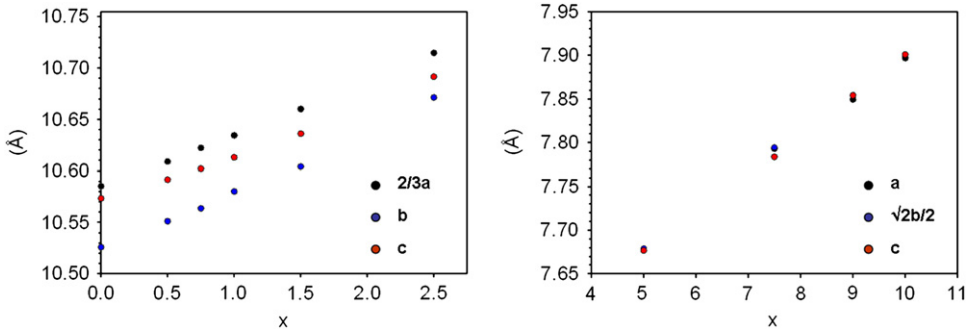

Fig. 6. Unit cell parameter *a*, *b* and *c*, as a function of lanthanum content, *x*, in $Y_{10-x}La_xW_2O_{21}$.

zone is intersecting the ewald sphere as a consequence of a short reciprocal lattice distance perpendicular to that direction. Analysis of the diffraction data revealed a unit cell of the superstructure that is $3 \times 2 \times 2$ that of the parent fluorite.

In Fig. 8(b), recorded from $Y_5La_5W_2O_{21}$, the micrograph shows a simpler superstructure, once again based on the [1 1 0] face centred cubic zone, but in this case the face centred cubic cell is doubled, possibly indicating a pyrochlore type structure.

The diffraction pattern presented in Fig. 8(c) was also recorded from $Y_5La_5W_2O_{21}$ and has a [1 1 4] face centred cubic zone with a doubled cell. However, in this case diffuse reflections can be seen pervading the pattern. This illustrates that the true structure is still more complex.

$La_{10}W_2O_{21}$ appears to have a doubled face centred cubic cell, as indicated partly in Fig. 8(d) and the lattice image reflects this. The image reveals that this is a reasonable interpretation and that extra reflections are real and not as a result of other features such as twinning.

3.4. Electrical measurements

The conductivity of the $Y_{10-x}La_xW_2O_{21}$ series determined from AC Impedance Spectroscopy measurements is summarised in Table 2. It should be noted that the density of most of the samples was low at 55–65% as a result of the low sintering temperature available for these refractory materials, 1600 °C, and this may introduce a minor error into the conductivity not accounted for by the simple density correction applied. However, the conduction processes and relative magnitudes are taken to be correct.

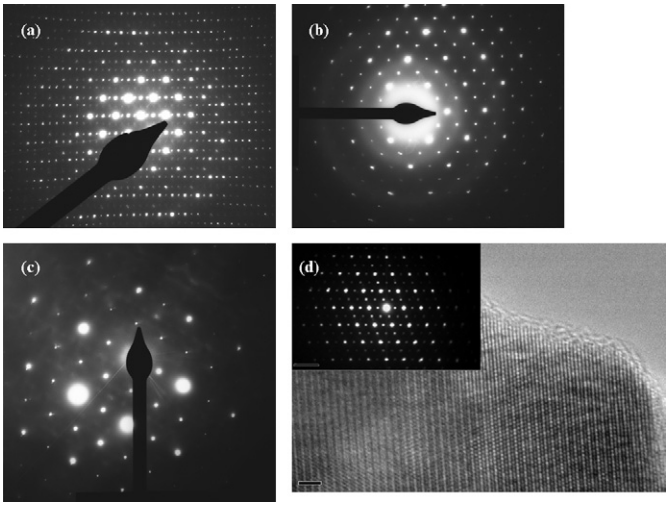

Fig. 8. (a) $Y_{10}W_2O_{21}$—strong reflections show the fluorite parent structure [1 1 0] type zone, and extra reflections indicate a superstructure [$3 \times 2 \times 2$] of the original fluorite cell, (b) $Y_5La_5W_2O_{21}$—stronger reflections once again show the fluorite parent [1 1 0] zone. However, in this case the superstructure is a simple doubling of the cell [$2 \times 2 \times 2$], possibly a pyrochlore related phase, (c) $Y_5La_5W_2O_{21}$—fluorite parent [1 1 4] type zone, showing superstructure doubling the cell, but with additional diffuse scatter suggesting that the structure is even more complex and (d) $La_{10}W_2O_{21}$—the [1 1 0] type fluorite zone showing a doubling of the cell indicating a pyrochlore type structure.

The end members, $Y_{10}W_2O_{21}$ and $La_{10+x}W_{2-x}O_{21-\delta}$ display a variation in their electrochemical behaviour. At 1000 °C $Y_{10}W_2O_{21}$ is an insulator and displays the lowest conductivity of 2×10^{-5} S cm^{-1}, whereas $La_{10+x}W_{2-x}O_{21-\delta}$ the highest at 3.7×10^{-3} S cm^{-1}and is an ionic conductor. The change in conductivity on increasing lanthanum content in these materials can be linked to the expansion of the unit cell and disorder on the cationic sublattice due to substitution of Y^{3+} by the larger La^{3+} ion.

Yttria rich samples with $0 \leq x \leq 5$ displayed high resistivity at 1000 °C, Fig. 9, in the order of $10^5\,\Omega$ cm, have the parent orthorhombic unit cell and are electronic insulators. In the lower temperature range 25–150 °C the samples all showed an increase in resistivity which is likely due to desorption of gases, primarily H_2O, as has been evidenced in the TGA data. From 150 to 1000 °C all are semiconducting. The conductivity of these samples at 25 °C decreases as a function of increasing La doping, and is consistent with the increasing activation energy observed for low temperature conductivity (Table 2). In contrast the conductivity at 1000 °C, increases as a function of increasing La content, as seen in Fig. 9, with the highest conductivity of 4×10^{-3} S cm^{-1}observed for $>75\%$ La content.

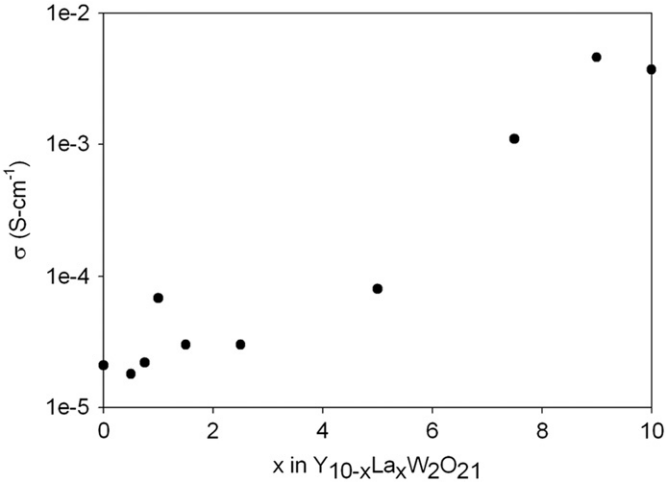

Fig. 9. Conductivity as a function of x in $Y_{10-x}La_xW_2O_{21}$ at 1000 °C.

Table 2
Conductivity and activation energy of $Y_{10-x}La_xW_2O_{21}$.

	σ (S cm^{-1}) in air at 1000 °C	Ea (eV) (T °C range measured)	σ (S cm^{-1}) in air at 25 °C	Ea (eV) (T °C range measured)	Density % at 1600 °C
$Y_{10}W_2O_{21}$	2.13E−05	1.63 (heating), 1.90 (cooling) 550–1000 °C	3.0E−07	1.05 (25–40)	57.6
$Y_{9.5}La_{0.5}W_2O_{21}$	4.4E−05	1.87 (1000–700)	9.3E−08	1.57 (25–40)	56.5
$Y_{9.25}La_{0.75}W_2O_{21}$	2.15E−05	0.84 (700–480), 1.43 (1000–700)	4.4E−08	_____	56.7
$Y_9LaW_2O_{21}$	6.8E−05	1.49 (500–1000)	7.6E−08	2.60 (24–35)	57.4
$Y_{8.5}La_{1.5}W_2O_{21}$	3.0E−05	1.8 (550–1000)	1.3E−08	_____	71.0
$Y_{7.5}La_{2.5}W_2O_{21}$	3.0E−05	1.96 (heating), 1.90 (cooling), 570–1000	1.0E−09	_____	94.6
$Y_5La_5W_2O_{21}$	8.04E−05	0.67 (400–700), 1.25(740–1000	_____	_____	66.5
$Y_{2.5}La_{7.5}W_2O_{21}$	1.10E−03	0.77 (300–1000)	6.0E−09	_____	66.3
$YLa_9W_2O_{21}$	4.56E−03	0.81 (200–1000) heating, 0.77 (200–1000) cooling	_____		87.8
$La_{10}W_2O_{21}$	3.74E−03	0.60 (200–500), 0.86 (750–1000)	_____	_____	62.2

The high resistivity of the yttria rich samples masked almost all low frequency contributions in the AC Impedance measurements at all but the highest temperatures; however there is a definite high capacitance element at low frequency above 800 °C. With increasing lanthanum content, $x \geq 5$, the unit cell becomes pseudo-cubic leading to disorder on the cation sites, and even at low temperatures the materials exhibit an extra Warburg diffusion element in the Nyquist plots, Fig. 8, characteristic of significant ionic conduction. Lanthanum tungstates are known for their ionic conductivity, in particular they were shown to have protonic conduction in humidified gas streams. Although the transport number has not been determined for the high lanthanum content samples in this study it is very likely that our composition $La_{10+x}W_{2-x}O_{21-\delta}$ is the same as the composition of the proton conductor erroneously reported in [6] as the high temperature phase La_6WO_{12}, however [6] lacks any structural data. At low temperatures the ionic conduction is therefore probably protonic to some degree and at temperatures above 800 °C in air the conduction is likely to be by oxide ions.

The conductivity of the lanthanum rich samples at 1000 °C increases two orders of magnitude from 8×10^{-5} to 4×10^{-3} S cm^{-1} as the unit cell expands on going from $Y_5La_5W_2O_{21}$ to $La_{10+x}W_{2-x}O_{21-\delta}$. The cell expansion coupled with the slight oxygen deficiency caused by segregation of the secondary phase would be expected to facilitate the migration of oxide ions and these are the proposed ionic charge carriers.

The density of lanthanum rich samples is generally higher than that of yttria rich samples, however, for most samples the low density made the deconvolution of the bulk and the resultant poor grain boundary contribution to the total conductivity impossible and yielded only a single broadened arc in the Nyquist plots. Even for the densest sample at 95% of theoretical, those of composition $Y_{7.5}La_{2.5}W_2O_{21}$, the bulk and the grain boundary are too highly correlated because of the low resistance of the grain boundaries and could not be separated; the results for the conductivity reported are to be taken as those of the bulk from the capacitance values observed.

The $La_{10+x}W_{2-x}O_{21-\delta}$ samples were the only exception where the bulk and the grain boundary were able to be separated up to 700 °C using a standard RC circuit model, Fig. 11. From the Arrhenius plot for $La_{10+x}W_{2-x}O_{21-\delta}$ in Fig. 12 it can be seen that the grain boundary is very conductive compared to the bulk, thus the bulk constitutes the majority of the total observed impedance. For example, at 700 °C the grain boundary resistivity is only 15 Ω cm, compared to the total resistivity of 3 kΩ cm.

The $Y_{10-x}La_xW_2O_{21}$ series are therefore from a family of ionic conductors and the highest conductivity of 4.6×10^{-3} S cm^{-1} at 1000 °C was observed for $YLa_9W_2O_{21}$ and is comparable to the un-optimised yttria stabilised zirconia at the same temperature.

Inspection of the Arrhenius plots for the all the phases synthesised, Fig. 10, and the data in Table 2, shows a change in conduction mechanism with increasing lanthanum content. Alternate points for each sample are heating and cooling and show that there is limited or no hysteresis, thus have been omitted for clarity.

At the yttria rich end of the compositional range either side of the two phases $Y_{9.25-9.0}$ the activation energy of the thermally activated conduction process is high, 1.8–1.9 eV, and corresponds in magnitude to Schottky defect formation. At the lanthanum end of the series the activation energy is 0.8 eV and is consistent with the migration enthalpy of oxide ions in perovskite (LSGM) and fluorite, (ZrO_2 and CeO_2) systems, however four terminal DC measurements as a function of pO_2 are required to confirm the nature of the charge carriers and the extent of the ionic regime.

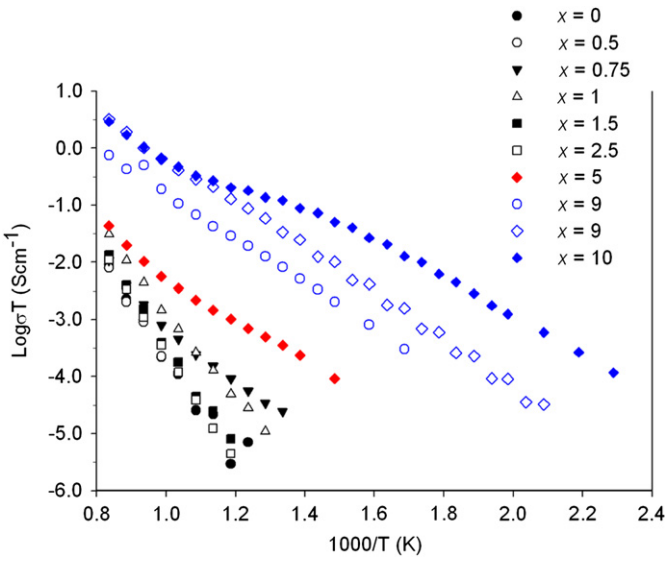

Fig. 10. Arrhenius plot for $Y_{10-x}La_xW_2O_{21}$ showing total conductivities.

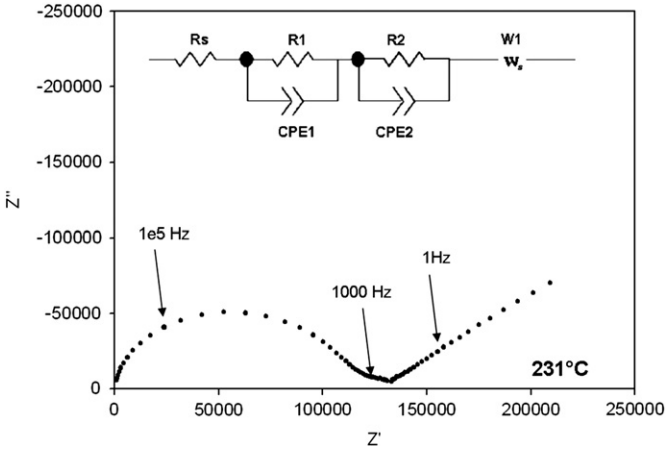

Fig. 11. Nyquist plot for $La_{10}W_2O_{21}$ at 231 °C with equivalent circuit model used, insert, showing the low frequency Warburg diffusion element, W1, characteristic of ionic conduction.

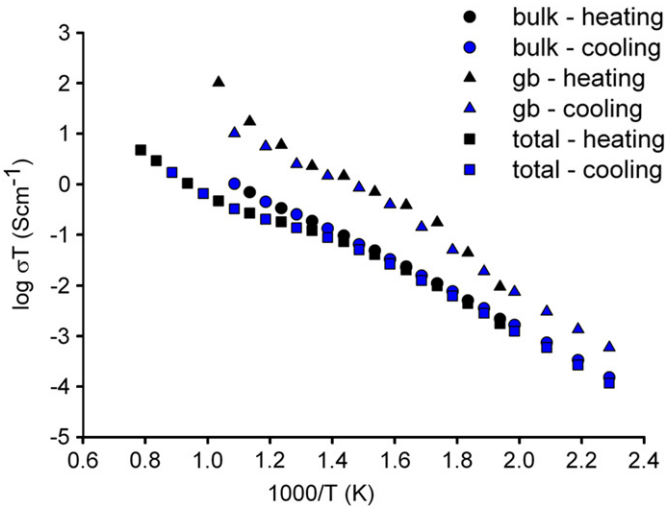

Fig. 12. Arrhenius plot for $La_{10+x}W_{2-x}O_{21-\delta}$, showing the bulk, the grain boundary and the total conductivity.

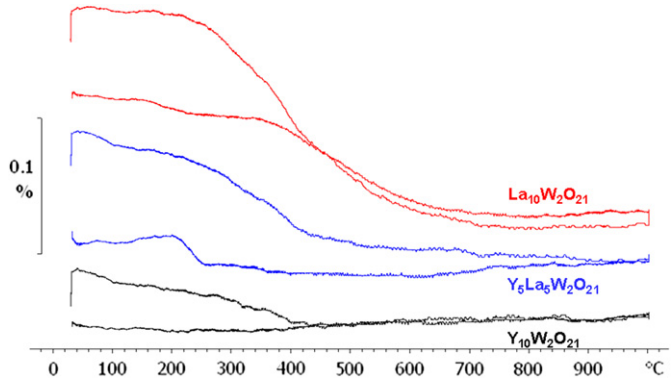

Fig. 13. Thermo-gravimetric analysis of $Y_{10-x}La_xW_2O_{21}$.

3.5. TGA/DTA

Weight loss was observed at 400–600 °C for La rich samples corresponding to possible H_2O desorption with a maximum 0.16% weight loss, Fig. 13. Upon cooling further weight gain corresponding to H_2O uptake was observed at 600–400 °C, and a smaller weight gain at 200–100 °C in La rich compounds. For yttria rich samples the gradual weight loss occurs at 100–400 °C. No weight increase was observed for $Y_{10}W_2O_{21}$ on cooling. For $Y_5La_5W_2O_{21}$ only a single weight gain step is observed at 200 °C, possibly indicating some water or CO_2 uptake.

The TGA shows that, as is typical for lanthanum compounds, some H_2O and CO_2 are absorbed in ambient conditions, however by 600 °C total dissociation is observed. The quantity of absorbed species is small, corresponding to a maximum of 0.16 wt% for $La_{10}W_2O_{21}$ and diminishing with increasing yttria content to a minimum of 3.7×10^{-2} wt% for $Y_{10}W_2O_{21}$.

3.6. Further doping studies and analogues

Additional doping was carried out using the same solid state synthesis procedure as described. Ta_2O_5 was chosen as a possible substitute for WO_3 due to the similar ionic radii in 6 fold coordination (0.64 and 0.60 Å, respectively), in order to evaluate if additional oxygen deficiency could be introduced into the structure. $Y_{10}W_{1.9}Ta_{0.1}O_{20.95}$ phase was synthesised at 1600 °C. However, tantalum was found to be insoluble in the parent phase structure and with the refined unit cell parameters being equivalent to those of pure $Y_{10}W_2O_{21}$, $a=15.8702\ (7)$ Å, $b=10.5339\,(4)$ Å and $c=10.5747\ (5)$ Å. The additional phase was found to be Ta_2O_5 (C12/c1), with increased unit cell parameters indicating limited possible Y_2O_3 substitution.

4. Conclusions

The structure and conductivity of the $Y_{10-x}La_xW_2O_{21}$ series was investigated with a view to examine novel materials with useful properties. It was found that the orthorhombic structure of $Y_{10}W_2O_{21}$ was distorted towards a pseudo-cubic structure of $Y_5La_5W_2O_{21}$ with increasing La content. Synchrotron data showed the cell to be orthorhombic $\sqrt{2}\times2\times\sqrt{2}$ fluorite units consistent with the weberite structure type. The disorder is believed to be due to the unique *Ln*4 site in $Y_{10}W_2O_{21}$, which is considered to be either eight-fold co-ordinate or a sixfold triangular-prismatic arrangement, and is thus an ideal acceptor site for a larger La^{3+} ion, which prefers eight-fold coordination. With increasing lanthanum substitution, at $x=7.5$, a secondary phase is observed, corresponding to $La_6W_2O_{15}$, however, lanthanum is further incorporated into the structure as is seen in a linear Vegard's law increase in the unit cell parameters as a function of x.

The conductivity of yttria rich samples was very low, with 10^{-5}–10^{-6} S cm^{-1} at 1000 °C, and ionic conductivity was observed for La doped samples. Increasing the lanthanum content increased the conductivity to 5×10^{-3} S cm^{-1}, and ionic conduction is seen for all samples. From the activation energies, the conduction process is believed to correspond to oxide ion conductivity.

References

[1] G.J. McCarthy, R.D. Fischer, Materials Research Bulletin 6 (7) (1971) 591–602.
[2] M. Yoshimura, F. Sibieude, A. Rouanet, M. Foex, Journal of Solid State Chemistry 16 (3–4) (1976) 219–232.
[3] M. Yoshimura, Journal of the American Ceramic Society 60 (1–2) (1977) 77–78.
[4] O. Beaury, J. Dexpert-Ghys, M. Faucher, P. Caro, Journal of Luminescence 18–19 (Part 1) (1979) 249–252.
[5] D.A. Woodcock, P. Lightfoot, C. Ritter, Journal of Solid State Chemistry 149 (1) (2000) 92–98.
[6] R. Haugsrud, Solid State Ionics 178 (7–10) (2007) 555–560.
[7] T. Shimura, S. Fujimoto, H. Iwahara, Solid State Ionics 143 (1) (2001) 117–123.
[8] R. Haugsrud, C. Kjolseth, Journal of Physics and Chemistry of Solids 69 (7) (2008) 1758–1765.
[9] M. Yoshimura, A. Rouanet, Materials Research Bulletin 11 (2) (1976) 151–158.
[10] D.J.M. Bevan, J. Drennan, H.J. Rossell, Acta Crystallographica Section B 38 (12) (1982) 2991–2997.
[11] O. Knop, T.S. Cameron, K. Jochem, Journal of Solid State Chemistry 43 (2) (1982) 213–221.
[12] M. Renninger, Zeitschrift Fur Kristallographie 97 (1/2) (1937) 95–106.
[13] L. Vegard, H. Dale, Zeitschrift Fur Kristallographie 67 (1928) 148–162.
[14] R.D. Shannon, C.T. Prewitt, Acta Crystallographica Section B 25 (5) (1969) 925–946.
[15] V.K. Yanovskii, V.I. Voronkova, Inorganic Materials 19 (3) (1983) 375–379.